Rashba spin-orbit coupling enhanced magnetoresistance in junctions with one ferromagnet

Chenghao Shen [1], Ranran Cai,[2] Alex Matos-Abiague,[3] Wei Han,[2] Jong E. Han,[1] and Igor Žutić [1]

[1]*Department of Physics, University at Buffalo, State University of New York, Buffalo, New York 14260, USA*
[2]*International Center for Quantum Materials, School of Physics, Peking University, Beijing 100871, People's Republic of China*
[3]*Department of Physics and Astronomy, Wayne State University, Detroit, Michigan 48201, USA*

We explain how Rashba spin-orbit coupling (SOC) in a two-dimensional electron gas (2DEG), or in a conventional *s*-wave superconductor, can lead to a large magnetoresistance even with one ferromagnet. However, such enhanced magnetoresistance is not generic and can be nonmonotonic and change its sign with Rashba SOC. For an in-plane rotation of magnetization, it is typically negligibly small for a 2DEG and depends on the perfect transmission which emerges from a spin-parity-time symmetry of the scattering states, while this symmetry is generally absent from the Hamiltonian of the system. The key difference from considering the normal-state magnetoresistance is the presence of the spin-dependent Andreev reflection at superconducting interfaces. In the fabricated junctions of quasi-2D van der Waals ferromagnets with conventional *s*-wave superconductors ($Fe_{0.29}TaS_2/NbN$) we find another example of enhanced magnetoresistance where the presence of Rashba SOC reduces the effective interfacial strength and is responsible for an equal-spin Andreev reflection. The observed nonmonotonic trend in the out-of-plane magnetoresistance with the interfacial barrier is an evidence for the proximity-induced equal-spin-triplet superconductivity.

I. INTRODUCTION

The magnetoresistance (MR) is a key figure of merit in spintronics and its enhancement is associated with the major advances in magnetically sensing and storing information [1–5]. Typically, a large MR is sought in structures with multiple ferromagnetic regions, where the resulting spin-valve effect implies that the resistance of the systems depends on the relative magnetization **M** orientation of those ferromagnets.

However, as first discovered in 1857 by Lord Kelvin [6], anisotropic MR (AMR) shows that with spin-orbit coupling (SOC) there is a change of the electrical resistivity with the relative direction of the charge current with respect to **M** of a single bulk ferromagnet (F), such as Ni or Fe. Another example of MR with a single F region is the tunneling AMR (TAMR) [7–10], also a manifestation of the interplay between SOC and **M**. Unfortunately, while a single F region simplifies scaled-down devices both AMR and TAMR are limited by their small magnitudes (typically <1 % for in-plane **M** rotation) [10,11].

In this work we explore a possibility for a much larger MR with a single F region and Bychkov-Rashba, also known as Rashba SOC [12], in both normal and superconducting states. The resulting enhanced MR is not only significant for the potential spintronic applications, but could also distinguish between the trivial and topological states [11], or provide a signature of equal-spin-triplet superconductivity, sought to realize coexistence of ferromagnetism and superconductivity, dissipationless spin currents, and Majorana bound states for fault-tolerant topological quantum computing [13–22].

To realize an enhanced normal-state MR, we consider a lateral geometry from Fig. 1(a). The resulting TAMR is not determined by highly spin-polarized carriers or a large

exchange energy in the F region, but by the high interfacial transmission from the interplay of the Rashba SOC, the barrier strength at the F/2DEG interface, and the proximity-induced exchange field, which can reach tens of meV and extend over tens of nm [23–27].

For a simple spinless case of a square barrier with thickness d and height V_0, a standard expression for transmission T with energy $E > V_0$ is [28,29]

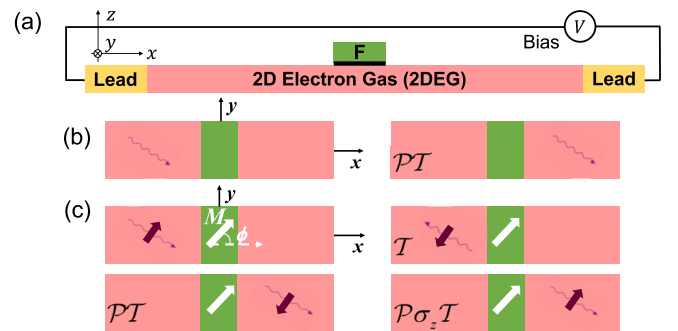$$T = \left(1 + V_0^2 \sin^2(kd)/[4E(E - V_0)]\right)^{-1}, \quad (1)$$

FIG. 1. (a) Lateral geometry, the current flows in the 2DEG. (b) Action of the time reversal $\mathcal{T}$ and the space-inversion operator $\mathcal{P}$ on the incident wave. By applying the $\mathcal{PT}$ operator, the incident wave on the left is transformed into a transmitted wave on the right. For a spinless barrier system, the $\mathcal{PT}$ symmetry gives the perfect transmission. (c) Action of the $\mathcal{P}\sigma_z\mathcal{T}$ operator and the $\mathcal{P}\sigma_z\mathcal{T}$ symmetry generalizes the condition from (b) for an incident wave with an in-plane spin and a barrier with the in-plane magnetization **M**, defined by the polar angle ϕ.

where $k = \sqrt{2m(E - V_0)}/\hbar$ is the wave vector. The perfect transmission $T = 1$ requires (i) $V_0 = 0$ or (ii) $kd = n\pi$, where $n = 1, 2, 3, \ldots$, gives the resonance condition. This well-known behavior [28,29] is usually not connected to the parity-time symmetry $\mathcal{PT}$, depicted in Fig. 1(b), which satisfies both cases (i) and (ii). Such a symmetry, where $\mathcal{P}$ is the parity operator, $\mathcal{T} = \mathcal{K}$ is the time-reversal operator, and $\mathcal{K}$ is the complex-conjugation operator, which ensures that the incoming and transmitted spinless waves are identical, up to a phase.

However, generalization of the perfect transmission for spin-$\frac{1}{2}$ carriers, where $\mathcal{T} = -i\sigma_y\mathcal{K}$, and σ_y is the Pauli matrix, is much less explored with SOC and magnetic barriers. It was recently found that the perfect transmission emerges when the eigenstates of the F/2DEG Hamiltonian, $H_{\text{F/2DEG}}$, satisfy $\mathcal{P}\sigma_z\mathcal{T}$, the spin-parity-time symmetry, where $[\mathcal{P}\sigma_z\mathcal{T}, H_{\text{F/2DEG}}] \neq 0$ [11]. Intuitively, the emerging perfect transmission for the eigenstates of $H_{\text{F/2DEG}}$ which satisfy $\mathcal{P}\sigma_z\mathcal{T}$ can be understood from Fig. 1(c). $\mathcal{T}$ reverses the spin and motion of the incident wave, while $\mathcal{P}\sigma_z$ inverts both the spin (through σ_z) and position (through $\mathcal{P}$) of the wave. By applying the $\mathcal{P}\sigma_z\mathcal{T}$ operator the incident wave on the left is transformed to itself, but as a transmitted wave on the right. Therefore, scattering states which are eigenfunctions of $\mathcal{P}\sigma_z\mathcal{T}$ experience perfect transmission. The resulting in-plane TAMR amplitude

$$\text{TAMR}_{\parallel} = \frac{G(\phi = 0) - G(\phi = \pi/2)}{G(\phi = \pi/2)}, \quad (2)$$

where the ϕ-dependent conductance G is the inverse of the resistance, $G = 1/R$, with ϕ defined in Fig. 1(c), can be enhanced by one or two orders of magnitude.

To study an enhanced out-of-plane MR in the superconducting state, we focus on the recent transport experiments in junctions of quasi-2D van der Waals (vdW) F with conventional s-wave superconductors (S) (Fe$_{0.29}$TaS$_2$/NbN) [30]. Compared to the normal-state MR, the key difference is the presence of Andreev reflection at the F/S interface with Rashba SOC. In this process an incoming electron is reflected as a hole and the Cooper pair enters the S region. With SOC, in addition to the conventional Andreev reflection, where the incoming and reflected particles have an opposite spin, a spin-flip or equal-spin Andreev reflection is also possible in which the incoming and reflected particles have the same spin [31,32]. While the first process is responsible for the spin-singlet proximity-induced superconductivity, the second yields the spin-triplet counterpart.

The corresponding anisotropic behavior, magnetoanisotropic Andreev reflection (MAAR) can be viewed as the generalization of TAMR [32–34], which is recovered in the normal state of the F/S junction for a large bias V, applied magnetic field B, or a high temperature. From a full MAAR calculation for the F/S junction, such a TAMR value can be obtained by taking the superconducting gap to vanish. Similar to Eq. (2), the out-of-plane MAAR amplitude in F/S junctions is

$$\text{MAAR}_{\perp} = \frac{G(\theta = 0) - G(\theta = \pi/2)}{G(\theta = \pi/2)}, \quad (3)$$

where θ is the angle defined in Fig. 2. As we later show, F/S measurements for the MAAR can be orders of magnitude
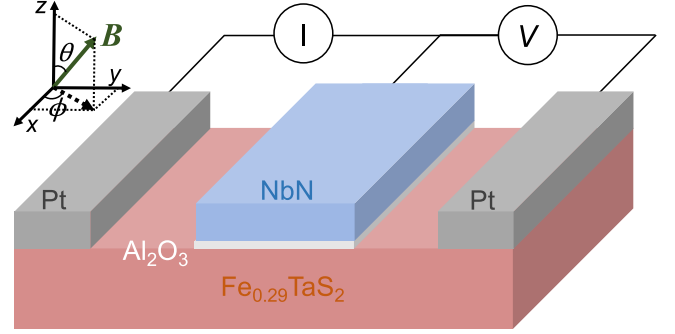

FIG. 2. Schematic of the geometry including a quasi-2D vdW F/S junction Fe$_{0.29}$TaS$_2$/NbN, with an Al$_2$O$_3$ insulating barrier. MR measurements are performed for an out-of-plane **M** rotation, defined by angle θ with respect to the applied magnetic field **B**. The interfacial resistance is obtained as V/I.

larger than TAMR in the normal state. This enhancement is dominated by the spin-flip Andreev reflection with Rashba SOC at the F/S interface.

Despite the different geometries for the considered F/2DEG and F/S structures, which also differ by the in-plane vs out-of-plane rotation of **M**, we find important common features and surprising nonmonotonic trends in TAMR in both systems. Some of these identified trends arise from the role of Rashba SOC which modifies the effective barrier strength and determines the condition for perfect transmission or an enhanced contribution of the spin-flip Andreev reflection.

Following this Introduction, we explore the structures from Fig. 1(a). In Sec. II we describe the F/2DEG Hamiltonian, consider the influence of SOC on the scattering states, and analyze the conductance which reveals different resonant-like behavior, peaked at different parameters. The calculation of in-plane TAMR in Sec. III reveals different trends as a function of the barrier and SOC strengths as well as the proximity-induced exchange splitting. In Sec. IV we examine the superconducting structures from Fig. 2 and describe the corresponding F/S Hamiltonian, followed by the measured and calculated conductance using a simple F/S Hamiltonian. In Sec. V we describe how the predicted influence of the Rashba SOC on the effective barrier strength provides a good description of the measured out-of-plane MR and confirms the evidence for the equal-spin-triplet superconductivity in the considered heterostructures. In Sec. VI we provide additional discussion for the relevance of enhanced MR in the normal and superconducting states and note some open questions for future work.

II. F/2DEG HAMILTONIAN AND CONDUCTANCE ANALYSIS

To explore the interplay of the proximity-modified two-dimensional electron gas (2DEG) and SOC, together with the magnetic anisotropy of the transport properties, we consider a model Hamiltonian of the system represented in Fig. 1(a)
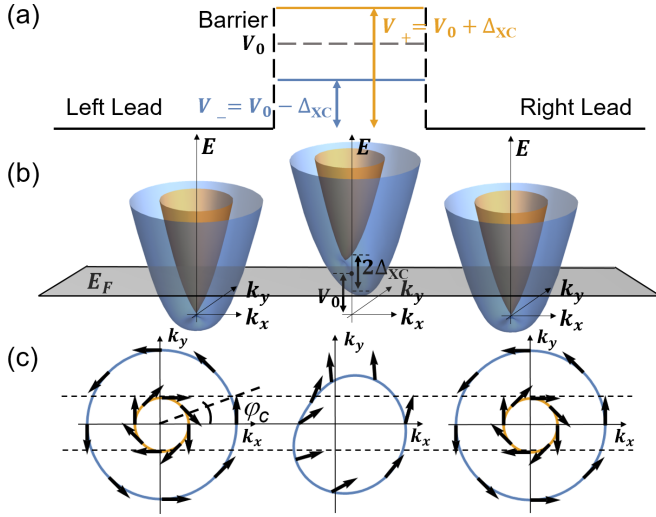
FIG. 3. (a) Schematic of the spin-dependent barrier. Its effective strength is modified by the proximity-induced exchange field Δ_{xc}, shown in a weak SOC limit. (b) 2DEG band structure with the Fermi energy E_F and the effective barrier region (middle) of height V_0 and Δ_{xc}. (c) Corresponding Fermi contours, arrows denote the spin orientation. Dashed lines: the range of a conserved wave vector k_y in the scattering states. For incident angles exceeding φ_c backscattering is suppressed.

given by

$$H_{\text{F/2DEG}} = \frac{p^2}{2m^*} + \frac{\alpha}{\hbar}(\boldsymbol{\sigma} \times \mathbf{p}) \cdot \hat{\mathbf{z}} + [V_0 - \Delta_{xc}(\mathbf{m} \cdot \boldsymbol{\sigma})]h(x), \tag{4}$$

where m^* is the effective mass, α is the Rashba SOC strength, $\hat{\mathbf{z}}$ is the unit vector along the z axis, $\mathbf{p} = (p_x, p_y)$ is the 2D momentum operator, $\boldsymbol{\sigma}$ is the vector of Pauli matrices, V_0 describes the potential barrier, Δ_{xc} and $\mathbf{m}$ are the magnitude and direction of the proximity-induced ferromagnetic exchange field. The function $h(x) = \Theta(d/2 + x)\Theta(d/2 - x)$ describes a square barrier of thickness d. We focus on electrons, not holes [35–38], with the effective barrier region and typical band structure shown in Fig. 3. In Fig. 3(a) the resulting spin-dependent barrier is shown in a weak SOC limit $\alpha k_F \ll \Delta_{xc}$, where $k_F = \sqrt{2m^*E_F}/\hbar$ is the Fermi wave vector averaged over the inner and outer contours in the leads, while E_F is the Fermi energy. The blue (yellow) contours in Fig. 3(c) denote lower (upper) bands. Inside the barrier the upper band is irrelevant since its bottom is above E_F. The spin orientations are marked by arrows.

Due to Rashba SOC, the wave functions can be classified by the helicity index, where $\lambda = 1 (-1)$ refers to the inner (outer) Fermi contour as depicted in Fig. 3(c). The scattering states for the finite square barrier model can be written as $\psi_\lambda(x, y) = (1/\sqrt{2A})e^{ik_y y}\phi_\lambda(x)$, with sample area A and the conserved parallel component of the wave vector k_y in the ballistic transport. Right from the barrier, $\phi_\lambda(x)$ is a combination of the two plane waves with transmission coefficients $t_{\lambda\lambda}$ and $t_{\lambda\bar{\lambda}}$, where $\bar{\lambda} = -\lambda$, to describe intraband and interband scattering processes.

By matching $\phi_\lambda(x)$ and $d\phi_\lambda(x)/dx$ in the regions $x < -d/2$, $-d/2 < x < -d/2$, and $x > d/2$, we obtain $t_{\lambda\lambda}$, $t_{\lambda\bar{\lambda}}$,

and the particle current density of the λ channel

$$j_\lambda = \text{Re}[v/A(|t_{\lambda\lambda}|^2 \cos \varphi_\lambda + |t_{\lambda\bar{\lambda}}|^2 \cos \varphi_{\bar{\lambda}})]. \tag{5}$$

Here, the group velocity of the scattered particle, $v = \sqrt{(\alpha/\hbar)^2 + 2E/m^*}$, has the same magnitude for the two bands. This current contains contributions from the intrachannel and interchannel transmissions, where φ_λ is the incident and $\varphi_{\bar{\lambda}}$ the propagation angle of the cross-channel wave with the conservation of the k_y component and $\varphi_{\bar{\lambda}}$ is related to φ_λ by $\cos \varphi_{\bar{\lambda}} = \sqrt{k_\lambda^2 - k_\lambda^2 \sin^2 \varphi_\lambda}/k_{\bar{\lambda}}$, where

$$k_\lambda = \sqrt{\left(\frac{\alpha m^*}{\hbar^2}\right)^2 + \frac{2m^*E}{\hbar^2} - \frac{\lambda \alpha m^*}{\hbar^2}}. \tag{6}$$

In the low-bias limit, i.e., $|eV| \ll E_F$, we get the expression for the conductance G_λ in the λ channel [39]

$$G_\lambda = \frac{e^2}{h} \frac{D}{2\pi} \int_{-\frac{\pi}{2}}^{\frac{\pi}{2}} d\varphi_\lambda k_F^\lambda T_\lambda \cos \varphi_\lambda, \tag{7}$$

where D is the sample width, k_F^λ the λ-channel Fermi wave vector [$E = E_F$ in Eq. (6)], and the transmission is

$$T_\lambda = \text{Re}[|t_{\lambda\lambda}|^2 + |t_{\lambda\bar{\lambda}}|^2 (\cos \varphi_{\bar{\lambda}} / \cos \varphi_\lambda)]. \tag{8}$$

The total conductance is the sum of the two channels,

$$G = \sum_{\lambda = \pm 1} G_\lambda. \tag{9}$$

To explore the evolution of the conductance as a function of the proximity-induced field and its direction, we consider its normalized value in Eq. (9) expressed in terms of the Sharvin conductance for the 2DEG system:

$$G_0^{2D} = \frac{e^2}{h} \frac{2D}{\pi} \sqrt{\left(\frac{\alpha m^*}{\hbar^2}\right)^2 + \frac{2m^* E_F}{\hbar^2}}. \tag{10}$$

As shown in Fig. 1(c), the $\mathcal{P}\sigma_z\mathcal{T}$ symmetry leads to perfect transmission and influences the conductance for the 2DEG system. Specifically, scattering states which satisfy $\mathcal{P}\sigma_z\mathcal{T}\psi(x, y) = \xi\psi(x, y)$, with eigenvalues of the form $\xi = e^{i\eta}$, include the perfect transmission either due to effectively vanishing barrier or the resonances expected from the standing-wave condition. However, $\mathcal{P}\sigma_z\mathcal{T}$ symmetry is not an intrinsic symmetry of the system and $\mathcal{P}\sigma_z\mathcal{T}$ does not commute with $H_{\text{F/2DEG}}$ in Eq. (4). Instead, the $\mathcal{P}\sigma_z\mathcal{T}$ symmetry emerges only for certain specific system parameters and scattering states satisfying

$$[H_{\text{F/2DEG}}, \mathcal{P}\sigma_z\mathcal{T}]\psi_R(x, y) = 0, \tag{11}$$

where the index R emphasizes that the relation is restricted only to the cases of the perfect transmission (for vanishing of the effective barrier or at resonances). This symmetry generalizes a simple case of the perfect transmission in a potential barrier (or a spinless) system [28].

To understand the relation between conductance, barrier parameters, and the perfect transmission, we perform a Fermi contour analysis illustrated in Fig. 4. In the spinless case, with the better matching between Fermi contours in the lead and barrier a higher transmission is expected. For a simple 1D
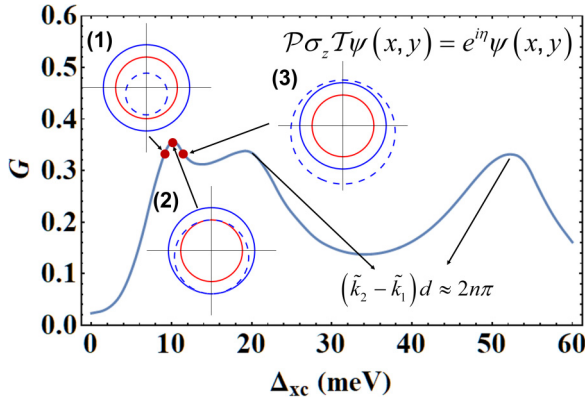
FIG. 4. Normalized conductance G as a function of Δ_{xc}, for $E_F = 5$ meV, $V_0 = 10$ meV, $\alpha = 0.093$ eV Å, and $d = 26$ nm. Fermi contours at different Δ_{xc}, $\mathbf{m} \parallel \mathbf{x}$: Blue and red circles are in the lead and the dashed contours in the barrier (only one band exists at the given E). Each of the three peaks in G satisfies the $\mathcal{P}\sigma_z\mathcal{T}$ symmetry for the perfect transmission.

geometry (normal incidence or a fixed k_y) and δ barrier, the transmission is [40]

$$T = 1/(1 + Z^2), \tag{12}$$

where Z is the effective barrier strength which combines the influence of a native barrier and the Fermi wave vectors mismatch in the two regions [31,33,41,42]. Since the difference between the lead and barrier Fermi contours is associated with the effective barrier potential, a larger mismatch between Fermi contours corresponds to a larger effective Z and thus to a lower transmission.

We now generalize this situation to a spin-dependent case in the presence of Δ_{xc} and α, as depicted in Figs. 3(b) and 3(c). The effective barrier at the F/2DEG interface becomes spin dependent since the energy bands in the barrier are split by the exchange field and spinless Z becomes $Z_\pm^{\mathrm{eff}}$ [33]. For the situation from Fig. 3, we can decompose the incident spinor in the basis constructed by the corresponding barrier eigenspinor ($k_{x,y}$ is the same as in the incident state) for the lower band $\chi_\uparrow$ and its antiparallel partner from the upper band $\chi_\downarrow$, i.e., $|\chi_{\mathrm{in}}\rangle = \langle\chi_\uparrow|\chi_{\mathrm{in}}\rangle|\chi_\uparrow\rangle + \langle\chi_\downarrow|\chi_{\mathrm{in}}\rangle|\chi_\downarrow\rangle$. The first term undergoes a weak effective barrier Z_-^{eff} while the second term experiences a strong barrrier Z_+^{eff}.

The effective interfacial barrier is inequivalent for two helicities (for outer and inner Fermi contours) leading to an important influence of spin mismatch on transmission, not just the mismatch of the Fermi contours [33]. Considering that the direction of the proximity-induced exchange field $\mathbf{m}$ [see Eq. (4)] is determined by ϕ, for an in-plane $\mathbf{M}$ as depicted in Fig. 1(c), the effective barrier for $|\chi_{\mathrm{in}}\rangle$ from the outer band of the lead is

$$Z_\pm^{\mathrm{eff}} \propto V_0 \pm \sqrt{(\alpha k_x + \Delta_{xc}\sin\phi)^2 + (\alpha k_y - \Delta_{xc}\cos\phi)^2} - \alpha k. \tag{13}$$

Equivalently, for $|\chi_{\mathrm{in}}\rangle$ from the inner band of the lead

$$Z_\pm^{\mathrm{eff}} \propto V_0 \pm \sqrt{(\alpha k_x + \Delta_{xc}\sin\phi)^2 + (\alpha k_y - \Delta_{xc}\cos\phi)^2} + \alpha k. \tag{14}$$

In Eqs. (13) and (14) the impact of the reflected states is neglected, and this treatment is most accurate for small effective Z, i.e., for a good matching of Fermi contours. We note that the effective barrier becomes energy dependent when $\Delta_{xc} \neq 0$ and $\alpha \neq 0$, opening the possibility for resonant tunneling to occur when the energy of the incident carrier is such that $Z_-^{\mathrm{eff}} \to 0$ (or $Z_+^{\mathrm{eff}} \to 0$).

Due to the spin mismatch, we need to include a correction of $|\langle\chi_\uparrow|\chi_{\mathrm{in}}\rangle|^2$ in the transmission, i.e., $T \approx |\langle\chi_\uparrow|\chi_{\mathrm{in}}\rangle|^2 T_{\chi_\uparrow}$, where $T_{\chi_\uparrow}$ is the transmission without the spin mismatch. We can see from Fig. 1(c) that the spin mismatch is much smaller for the incident state from the outer lead band ($\lambda = -1$), i.e., $|\langle\chi_\uparrow | \chi_{\mathrm{in}}, \lambda = -1\rangle| \gg |\langle\chi_\uparrow | \chi_{\mathrm{in}}, \lambda = 1\rangle|$, which indicates that the most of G is contributed by the incident states from the outer lead band. When the state inside the barrier is the same (up to a phase) as that in the lead, perfect transmission is achieved.

With vanishing Rashba SOC, $\alpha \to 0$, outer and inner lead Fermi contours coincide and the spin-dependent barrier $V_\pm = V_0 \pm \Delta_{xc}$ from Fig. 3(a) is recovered. We focus on $V_0 > 0$, $V_- = 0$ leads to the perfect transmission $T_{\chi_\uparrow} = 1$ from our discussion above. From Eqs. (13) and (14), $Z_\pm^{\mathrm{eff}} \propto V_0 \pm \Delta_{xc}$, so one can still get $Z_-^{\mathrm{eff}} \to 0$ when $V_0 = \Delta_{xc}$. We will further address the importance of vanishing V_- in F/S junctions. At a fixed k_y, the eigenstate for the perfect transmission $T(k_y) = 1$ precisely satisfies the $\mathcal{P}\sigma_z\mathcal{T}$ symmetry: $\mathcal{P}\sigma_z\mathcal{T}\psi(x, y) = \xi\psi(x, y)$, with eigenvalue $\xi = e^{i\eta}$ and an arbitrary phase η.

This analysis and the relevance of the $\mathcal{P}\sigma_z\mathcal{T}$ symmetry can be applied to Fig. 4 with parameters of a typical InGaAs/InAlAs 2DEG, $m^* = 0.05m_0$, where m_0 is the free-electron mass, and $\alpha = 0.093$ eV Å [43]. It is crucial to note that $\mathcal{P}\sigma_z\mathcal{T}$ symmetry arguments for a perfect transmission pertain to a single k_y (single channel), while the geometry from Figs. 1(a) and 3 corresponds to a 2D system where the total G reflects the contribution from all allowed k_y. In the spinless case, maximizing G means an overall contour matching, while even with adding spin our Fermi contour analysis provides a valuable tool to visualize and understand various trends in G.

With conserved k_y, from Fig. 3(c) we can recognize many similarities with Snell's law [42]. We may get propagating or decaying (evanescent) states in different regions, depending on the incident angle φ and the particular contour (outer, inner) considered. For example, for carriers from the $\lambda = -1$ band (outer contour) and incident angles φ exceeding the critical angle,

$$\varphi_c = \pm\arcsin(k_1/k_{-1}), \tag{15}$$

where $k_\lambda = \pm 1$ is given by Eq. (6), the transmission and reflection to the $\lambda = 1$ band are not allowed because there are no such propagating states. In this regime, backscattering is suppressed while $T_{\lambda=-1}$ is enhanced.

The overall maximum in $G(\Delta_{xc})$ is related to the perfect transmission due to the Fermi contour matching depicted by the example (2) in Fig. 4. As shown for examples (1) and (3) a small change in Δ_{xc} leads to worse Fermi contour matching and reduced G. The origin of the overall peak in G near $\Delta_{xc} = V_0$ can be further understood in the small SOC limit. The barrier contour reduces to a shifted circle with radius

$k_F \sqrt{(E_F + \Delta - V_0)/E_F}$, where we recall that k_F is average of the outer and inner lead circles. The barrier contour can then be approximated by

$$[k_x - (m^*\alpha/\hbar^2)\sin\phi]^2 + [k_y + (m^*\alpha/\hbar^2)\cos\phi]^2$$
$$\approx (2m^*/\hbar^2)(E_F + \Delta - V_0). \qquad (16)$$

In the region near the $\Delta_{xc} = V_0$, both $G(\phi = 0)$ and $G(\phi = \pi/2)$, which correspond to $\mathbf{m} \parallel \mathbf{x}$ and $\mathbf{m} \parallel \mathbf{y}$, reach their maxima because of the best matching of Fermi contours between lead and barrier. The shift of barrier circle is always $\perp$ to $\mathbf{m}$ and is of the first order in α, while the deformation is a higher-order correction.

Remarkably, the other local maxima in G, for larger Δ_{xc} in Fig. 4, also satisfy the $\mathcal{P}\sigma_z\mathcal{T}$ symmetry. However, instead of the contour matching, they are due to standing de Broglie waves in the barrier and the constructive interference. With outer and inner lead contours, there are four eigenstates in the leads with $\pm k_{x\lambda}$, $\pm k_{x\tilde{\lambda}}$, we can distinguish the following cases: (i) 4 (4), (ii) 4 (2), (iii) 2 (4), and (iv) 2 (2) propagating states in the leads (barrier) [11].

In cases (i) and (ii) (arising for an incident state from the inner band of for the outer band and $\varphi < \varphi_c$), the perfect transmission means that no reflected wave should exist in the left lead, while the state in the right lead should match, up to a phase, the corresponding one in the left lead. For case (i), under $\mathcal{P}\sigma_z\mathcal{T}$ symmetry operation, up to a phase, all the propagating states inside the barrier, with x component of the wave vector $\tilde{k}_j$, $j = 1, \ldots, 4$, remain the same. By matching $\phi_\lambda(x)$ and $d\phi_\lambda(x)/dx$, as noted in Sec. II, the resonance condition is satisfied when

$$(\tilde{k}_j - \tilde{k}_1)d = 2\pi n_j, \quad j = 2, 3, 4 \qquad (17)$$

where $n_j = 1, 2, \ldots$. However, for the system we consider, $\tilde{k}_j d \sim 10$ and Eq. (17) only holds in few special cases.

In case (ii) the resonance condition similar to Eq. (17) is not possible, unless for the normal incidence when $\mathbf{m} \parallel \mathbf{y}$. In that case, the coefficients of the decaying barrier states vanish and the spins of all scattering states become parallel to each other which makes the system "spinless" and perfect transmission becomes possible.

In cases (iii) and (iv), the presence of the decaying states in the leads can be understood for the incident particle from the $\lambda = -1$ band at an angle $\varphi > \varphi_c$. Since such decaying states in the leads do not carry any current [42], as can be understood from the Snell's law, the perfect transmission and the resonance conditions are still possible. In case (iv), under the symmetry $\mathcal{P}\sigma_z\mathcal{T}$ operation, up to a phase, the two propagating states inside the barrier remain the same, while the two decaying states in the barrier become, up to a phase, the two decaying states in the leads. The resonance condition is

$$(\tilde{k}_2 - \tilde{k}_1)d = 2n\pi - \delta, \quad n = 1, 2, 3\ldots \qquad (18)$$

where for the x component of the propagating wave vectors in the barrier we assume $\tilde{k}_2 > \tilde{k}_1$, while the correction $\delta \propto (\alpha/\hbar)\sqrt{m^*/\Delta_{xc}} \ll 1$. Since the resonances occur at $\Delta_{xc} > E_F$, the magnitude of the propagating barrier wave vector is much larger than k_y. Therefore, the x component of the propagating barrier wave vector is almost the same for all the incoming states with different incident angles, which means

the transmission resonances occur for all the incoming states almost simultaneously when the resonance condition is satisfied and thus the maximum G is reached.

The two local maxima in G near $\Delta_{xc} = 20$ and 55 meV, shown in Fig. 4, both correspond to the case (iv) and a large Δ_{xc} regime, where for $\mathbf{m} \parallel \mathbf{x}$ the propagating wave vectors are $\tilde{k}_{1,2} \approx \mp\sqrt{2m^*\Delta}/\hbar$. Applying the resonance condition from Eq. (18) the first (second) of these maxima corresponds to $n = 1$ ($n = 2$). However, with large Δ_{xc}, the correction δ in Eq. (18) is very small such that the resonance condition is accurately described by the spinless case where $\delta = 0$.

III. F/2DEG IN-PLANE TAMR

A large value of TAMR, as defined in Eq. (2), has the origin in the difference for the maximum $G(\phi = 0)$ and $G(\phi = \pi/2)$, that is for the $\mathbf{m} \parallel \mathbf{x}$ and $\mathbf{m} \parallel \mathbf{y}$ orientations. In Fig. 4, for $G(\phi = 0)$ and shown examples (1)–(3), we see the expected barrier Fermi contour (broken line) shifted downward ($\perp \mathbf{x}$). This broken k_y symmetry leads to an unusual tunneling planar Hall effect, where the transverse voltage is maximum for the $\mathbf{M} \parallel \mathbf{x}$, while other Hall effects would vanish [44]. Due to the same asymmetry, the perfect match for both upper and lower halves of the circle cannot be achieved simultaneously. We see in examples (1)–(3) that the upper (lower) half of the barrier contour tends to match the inner (outer) lead contour since the spin mismatch is smaller for these states. The best possible simultaneous match of Fermi contours yields the large transmission at $\Delta_{xc} = V_0$, resulting in the first peak in G, even for large α when the barrier contour is strongly deformed from a circle, as in Fig. 3(c).

As we see from Fig. 4 with multiple peaks in G, there also exist several resonances which could influence the TAMR. In the limit of $\alpha \to 0$, the condition for such resonances can be derived from Eq. (18) with $\delta = 0$

$$\Delta_{xc} = V_0 - E_F + \frac{\pi^2 \hbar^2 n^2}{2m^* d^2}, \qquad (19)$$

for both $G(\phi = 0)$ and $G(\phi = \pi/2)$ which correspond to $\mathbf{m} \parallel \mathbf{x}$ and $\mathbf{m} \parallel \mathbf{y}$, where $n = 1, 2, \ldots$ describes the order of the resonance that pertains to the case (iv) in Sec. II. In this situation, of vanishing Rashba SOC, the conductance no longer depends on the in-plane $\mathbf{m}$ and we expect a vanishing TAMR, as inferred from Eq. (2).

However, already for a small and nonvanishing α the maximum $G(\phi = \pi/2)$ is achieved for a different condition when the barrier circle shares the same size as the outer circle of the lead [11]. Up to the first order in α the condition leading to the maximum $G(\phi = \pi/2)$ is given by $\Delta_{xc} = V_0 + \alpha k_F$. When such a condition is satisfied, the barrier Fermi contour matches the outer lead contour instead of the inner one because the main G contribution is from the incident particles on the outer Fermi contour. Correspondingly, near $\Delta_{xc} = V_0$, due to contour matching and the perfect transmission, we expect enhanced TAMR, as can be seen from Fig. 5.

Furthermore, when $\alpha \neq 0$, $\tilde{k}_2 - \tilde{k}_1$, which determine the resonance condition in Eq. (18), varies as $\mathbf{M}$ is rotated. This means the maxima for $G(\phi = 0)$ and $G(\phi = \pi/2)$ will be achieved at different Δ_{xc}. Therefore, similar to the situation near $\Delta_{xc} = V_0$, an enhanced TAMR will arise from the small
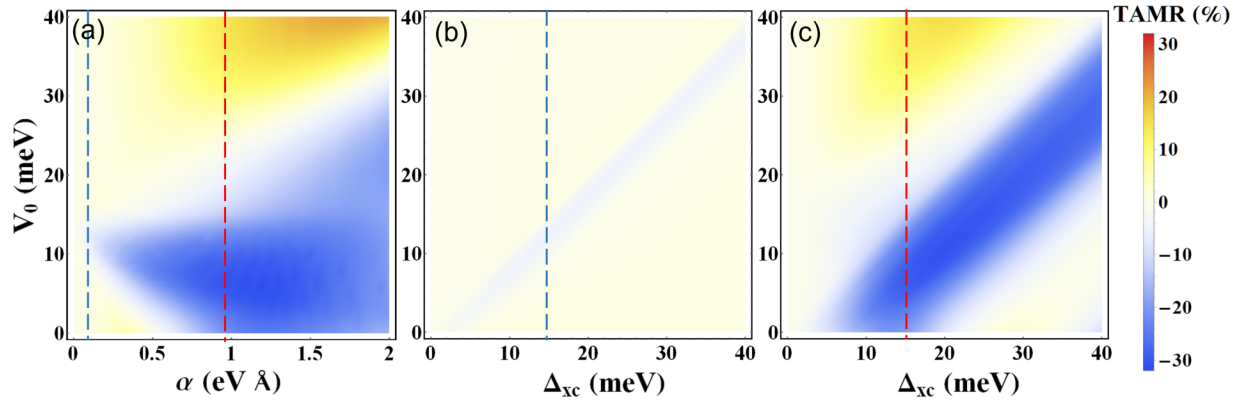
FIG. 5. (a) Dependence of the TAMR amplitude on the Rashba SOC α and the barrier strength V_0 for a 2DEG system with a $d = 13$ nm thick barrier, $E_F = 10$ meV, and proximity-induced exchange splitting $\Delta_{xc} = 15$ meV. (b) Dependence of the TAMR amplitude on Δ_{xc} and V_0, for the same d and E_F as in (a), with $\alpha = 0.093$ eV Å for a typical InGaAs/InAlAs 2DEG. (c) The same as (b), but $\alpha = 0.93$ eV Å. The blue and red dashed lines in (a) are for the same parameters as the ones in (b) and (c).

difference in the peak conditions. With fixed E_F and V_0, up to the lowest-order correction of α, we can derive the difference in Δ_{xc} at the same order maxima (n) of $G(\phi = 0)$ and $G(\phi = \pi/2)$:

$$\Delta_{xc}^{\text{diff}} \propto \alpha^2 m^*/\hbar^2. \tag{20}$$

Unlike the perfect transmission condition due to contour matching, the difference is now quadratic in α.

With this conductance analysis and nonmonotonic $G(\Delta_{xc})$ in Fig. 4, a consequence of the collective contributions of multiple $T \approx 1$ states corresponding to different propagation directions of the tunneling carriers, we expect various nonmonotonic TAMR trends and a strong influence of Rashba SOC. We can see from Fig. 5(a) that increasing α can enhance both TAMR and the range of V_0 for such enhancement. However, if α gets too large (>1.5 eV Å), the absolute value of TAMR decreases, for a large range of V_0.

The reason for this unexpected trend in TAMR(α) can be understood from calculated results in Figs. 5(b) and 5(c), which are shown for two different values of α, as indicated by blue and red vertical lines in Fig. 5(a). From the previous discussion of a small-α limit, we know that G peaks near $\Delta_{xc} = V_0$ and such a peak will be shifted by αk_F when $\mathbf{M}$ is rotated. The sensitive dependence of G on the $\mathbf{M}$ orientation leads to a large TAMR near the diagonal line in the parameter space, shown in Figs. 5(b) and 5(c). Since such a shift is proportional to α, by comparing Figs. 5(b) and 5(c) there is a wider range of the enhanced TAMR for a larger α.

However, if α is too large (compared to V_0/k_F and Δ_{xc}/k_F), the impact of the $\mathbf{M}$ orientation becomes negligible, and TAMR starts to decrease. This can be seen at the lower-left corner in Fig. 5(c), where the resonant TAMR is much smaller when both V_0/k_F, $\Delta_{xc}/k_F < \alpha$. Even for a fixed V_0, for example at 5 meV, we see that with α the absolute value of TAMR is nonmonotonic and TAMR also changes sign.

The calculated in-plane TAMR reveals various other peculiar trends. For a fixed α [Fig. 5(a)] or Δ_{xc}/k_F [Figs. 5(b) and 5(c)], we can see that TAMR can be nonmonotonic in V_0 and even change its sign. Furthermore, there is as a clear nonmonotonic amplitude with Δ_{xc} at a fixed V_0 in Fig. 5(b).

Different barrier thickness in Fig. 5 (26 nm) from that in Fig. 4 (13 nm) modifies the respective Δ_{xc} values for the perfect transmission. These different TAMR trends in Fig. 5 were primarily related to the best contour matching, near $\Delta_{xc} = V_0$ [as the first peak in G, seen in Fig. 4], while the role of $n = 1$ resonance can be seen in the lower-right corner in Fig. 5(c).

From the angular dependence of TAMR, it is possible to obtain valuable information about the interfacial crystallographic symmetry [23]. For a 2DEG system, in the limit and $\Delta_{xc}/V_0 \ll 1$, the leading contribution to the in-plane angular dependence of G from the two incoming channels with helicity $\lambda = \pm 1$ is $\pm \sin \phi$. However, with their opposite signs, these leading contributions cancel in the total G, which becomes significantly smaller, quadratic in the small parameter, and has a different angular dependence, resulting in

$$\text{TAMR}_{\text{F/2DEG}}(\phi) \sim (\Delta_{xc}/V_0)^2 \sin^2 \phi. \tag{21}$$

While this angular dependence also coincides with the results from the surface states of 3D topological insulators, their junctions with ferromagnets do not have a resonant TAMR behavior of a 2DEG and thus lead to different trends in Δ_{xc} and V_0 [11].

Another striking signature of the underlying resonant behavior of the calculated TAMR is its magnitude. In commonly considered vertical tunneling devices, the in-plane TAMR is rather small (typically $<1\%$) even for large carrier spin polarization [7] and exchange energies $>$ eV [8,45,46]. In contrast, with much smaller proximity-induced exchange fields $\Delta_{xc} \sim 10$ meV, we find a much larger TAMR in our lateral (planar) structures $>10\%$ even for SOC for a typical InAs-based 2DEG.

As we next focus on the F/S junctions and their superconducting out-of-plane TAMR analog [recall Eq. (3)], we will see that some of the calculated nonmonotonic trends, similar to those we discussed for F/2DEG systems, are experimentally verified, while the analysis of effective barriers allows us to give simple estimates of the enhanced MR which can even reach 100% in the measured samples.

IV. F/S HAMILTONIAN AND CONDUCTANCE

Motivated by the recent experiments demonstrating a large MR enhancement in F/S junctions [30], depicted in Fig. 2, we consider a simple model for F/S Hamiltonian $H_{\text{F/S}}$. It shares several similarities with $H_{\text{F/2DEG}}$ in Eq. (4), used to analyze in-plane TAMR. The key difference in the superconducting state is the need to simultaneously include the presence of electrons and holes and the pair potential Δ, which couples electronlike and holelike components of the underlying wave function.

Additionally, while Rashba SOC was inherent for whole 2DEG region, in F/S junction it is only an interfacial contribution, along with the potential barrier, between F and S regions. Now we study vertical transport and out-of-plane MR [recall Eq. (3)], which is dominated by the process of Andreev reflection, introduced in Sec. I and it is the microscopic mechanism for the superconducting proximity effects [23].

Before specifying $H_{\text{F/S}}$ and the resulting equation for quasiparticle states, it is instructive to note a similarity between the two-component transport in normal-metal (N)/S junctions (for electronlike and holelike quasiparticles) and F/N junctions (for spin $\uparrow$, $\downarrow$), which both lead to current conversion, accompanied by additional boundary resistance [3]. In the N/S junction Andreev reflection is responsible for the conversion between the normal and the supercurrent, characterized by the superconducting coherence length, while in the F/N case a conversion between spin-polarized and unpolarized currents is characterized by the spin diffusion length. In the N/S charge transport, Δ, which couples electronlike and holelike states, plays a similar role of the spin-flip potential which couples $\uparrow$, $\downarrow$ states in the F/N spin transport.

We consider ballistic F/S junction, depicted in Fig. 2, having a flat interface at $z = 0$ with potential and Rashba SOC scattering. Similar to the approach in Sec. II of matching the wave functions for the scattering states in different regions, we generalize the Griffin-Demers-Blonder-Tinkham-Klapwijk formalism [40,47–49] to solve Bogoliubov–de Gennes equation for quasiparticle states $H_{\text{F/S}}\Psi(\boldsymbol{r}) = E\Psi(\boldsymbol{r})$, with energy E [32], where

$$H_{\text{F/S}} = \begin{pmatrix} H_e & \Delta\Theta(z)I_{2\times2} \\ \Delta^*\Theta(z)I_{2\times2} & H_h \end{pmatrix}, \quad (22)$$

with Δ the s-wave pair potential which, for a homogeneous S region, is also the value of the superconducting gap, and the single-particle Hamiltonian for electrons is

$$H_e = -\frac{\hbar^2}{2}\nabla\frac{1}{m(z)}\nabla - \mu(z) - \Delta_{\text{xc}}(\boldsymbol{m}\cdot\boldsymbol{\sigma})\Theta(-z) + H_B, \quad (23)$$

while for holes $H_h = -\sigma_y H_e^* \sigma_y$. In Eq. (22), $m(z)$ is the effective mass and $\mu(z)$ is the chemical potential. The interfacial scattering is modeled by deltalike potential barrier, with the effective barrier height V_0 and width d and the interfacial Rashba SOC of strength α has different units than Rashba SOC in F/2DEG [8]:

$$H_B = [V_0 d + \alpha(k_y \hat{\sigma}_x - k_x \sigma_y)]\delta(z). \quad (24)$$

As in Sec. II, Δ_{xc} is the exchange spin splitting and we denote the orientation of the magnetization $\mathbf{M}$ by $\mathbf{m}$,

but we now also consider its out-of-plane rotation $\mathbf{m} = (\sin\theta\,\cos\phi, \sin\theta\,\sin\phi, \cos\theta)$.

Since the in-plane wave vector $\boldsymbol{k}_\parallel$ is conserved, the scattering states for incident spin σ electron are given by $\Psi_\sigma(\boldsymbol{r}) = e^{i\boldsymbol{k}_\parallel\cdot\boldsymbol{r}}\psi_\sigma(z)$ in a four-component basis, they include Andreev and specular reflection, each without and with spin flip, given by the amplitudes a_σ, b_σ, $\bar{a}_\sigma$, and $\bar{b}_\sigma$ [31].

In the F region, the eigenspinors for electrons and holes are $\chi_\sigma^e = (\chi_\sigma, 0)^T$ and $\chi_\sigma^h = (0, \chi_{-\sigma})^T$ with

$$\chi_\sigma = (1/\sqrt{2})(\sigma\sqrt{1 + \sigma\,\cos\theta}\,e^{-i\phi}, \sqrt{1 - \sigma\,\cos\theta})^T, \quad (25)$$

where $\sigma = 1\,(-1)$ or $\uparrow\,(\downarrow)$ refer to spin parallel (antiparallel) to $\mathbf{M}$ and the z components of the wave vector are

$$k_\sigma^{e\,(h)} = \sqrt{k_F^2 + \frac{2m_F}{\hbar^2}[(-)E + \sigma\Delta_{\text{xc}}] - k_\parallel^2}, \quad (26)$$

with a spin-averaged Fermi wave vector k_F [42]. At an interface, with conserved $\boldsymbol{k}_\parallel$, the H_B barrier eigenspinors in the helicity basis are given by [10,50]

$$\chi_\pm = \frac{1}{\sqrt{2}}\begin{pmatrix} 1 \\ \mp ie^{i\gamma} \end{pmatrix}, \quad (27)$$

where γ is the angle between $\boldsymbol{k}_\parallel$ and $\hat{\boldsymbol{k}}_x$.

In the S region, coherence factors u, v satisfy $u^2 = 1 - v^2 = (1 + \sqrt{E^2 - \Delta^2}/E)/2$, while the z components of the wave vector are

$$q^{e\,(h)} = \sqrt{q_F^2 + (-)\frac{2m_S}{\hbar^2}\sqrt{E^2 - \Delta^2} - k_\parallel^2}, \quad (28)$$

with q_F the Fermi wave vector. Similar to Snell's law [42], for a large $k_\parallel$ these z components can become imaginary representing evanescent states which carry no net current. The vanishing of evanescent states at infinity requires $\text{Im}[k_\sigma^h] < 0$, so the sign of the z component of the wave vectors needs to be chosen correctly.

From the charge-current conservation, the zero-temperature differential conductance at applied bias V can be expressed as [32]

$$G(V) = \sum_\sigma \int \frac{d\boldsymbol{k}_\parallel}{2\pi k_F^2}\left[1 + R_\sigma^h(-eV) - R_\sigma^e(eV)\right]. \quad (29)$$

Here $G(V)$ is normalized by the Sharvin conductance [3]

$$G_0^{\text{3D}} = \frac{e^2 k_F^2 A}{2\pi h}, \quad (30)$$

where A is the interfacial area, while the form is different than the previous expression in 2D [recall Eq. (10)], where SOC is present in the whole 2D region, not just at an interface. Only the probability amplitudes from the F region are needed for Andreev $R_\sigma^h = \text{Re}[(k_{-\sigma}^h/k_\sigma^e)|a_\sigma|^2 + (k_\sigma^h/k_\sigma^e)|\bar{a}_\sigma|^2]$ and specular reflection $R_\sigma^e = \text{Re}[|b_\sigma|^2 + (k_{-\sigma}^e/k_\sigma^e)|\bar{b}_\sigma|^2]$. A finite-temperature correction is straightforward by adding Fermi functions in Eq. (29), which smear the calculated $G(V)$ at $T = 0$ K. The integration kernel in Eq. (29) $[1 + R_\sigma^h - R_\sigma^e]$ can be viewed as the effective transmission.

We now turn to the measured bias dependence for differential conductance dI/dV for a quasi-2D vdW F/S junction (recall its geometry in Fig. 2), shown in Fig. 6(a) for several T. Some trends are expected: dI/dV peaks reflect the peaks
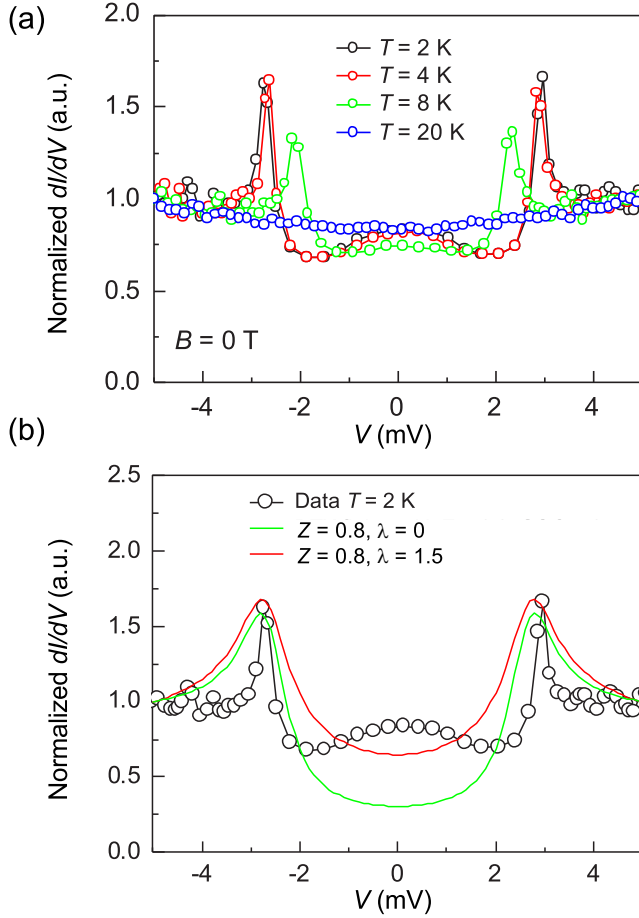
FIG. 6. (a) Measured and (b) calculated finite temperature and $B = 0$ differential conductance for $Fe_{0.29}TaS_2/NbN$ junction, normalized to its value at $V = 5$ mV, corresponding to the normal-state result. For $T = 2$ K comparison, in our calculations we choose $T/T_c = 0.16$, $P = 0.42$, and $\Delta = 2.7$ meV.

in the density of states, near $|eV| = \Delta$ [40], moving inward with T as $\Delta(T)$ is also suppressed with T. While the perfect transmission in 1D N/S geometry near $V = 0$ implies the doubling of the normal-state conductance [40], since an incident electron through Andreev reflection contributes to the transfer of an electron pair across the N/S interface, the F/S transmission should be diminished, both by the interfacial barrier, parametrized by Z [recall Eq. (12)], as well by the spin polarization $P = \Delta_{xc}/\mu_F \approx 0.4$–$0.5$, expected for $Fe_{0.29}TaS_2$ and measured in a similar $Fe_{0.26}TaS_2$ ferromagnet [51]. Only a fraction of the incident majority-spin electrons can find the opposite spin partner for Andreev reflection [42,52].

With the NbN critical temperature $T_c = 12.5$ K, we focus on dI/dV at the lowest $T = 2$ K and theoretically explore the role of interfacial properties using dimensional parameters for barrier strength and Rashba SOC:

$$Z = V_0 d \sqrt{m_F m_S}/(\hbar^2 \sqrt{k_F q_F}), \quad (31)$$

$$\lambda = 2\alpha \sqrt{m_F m_S}/\hbar^2. \quad (32)$$

Since we are interested in identifying trends with these interfacial parameters, rather than obtaining the best fit for

$dI(V)/dV$, we further simplify this approach by considering the case for $m_F = m_S = m$ and $k_F = q_F$.

Our calculated results are given in Fig. 6(b) and reflect these simplifications. For example, assuming that $k_F = q_F$ and that m is the free-electron mass, the chosen dimensionless barrier strength $Z = 0.8$ corresponds to $k_F = 1.4 \times 10^{10}$ m^{-1}, consistent with NbN values [53], while $V_0 = 0.5$ eV, and $d = 1.7$ nm is an average thickness among our studied F/S samples. The value of Rashba SOC, $\alpha = 5.7$ eV Å^2, which follows from the choice of $\lambda = 1.5$, is also consistent with separate fits of the angular dependence of MR measured near zero bias in Ref. [30].

By comparing $\lambda = 0$ and 1.5 results at a fixed $Z = 0.8$ above the gap the changes are very small. However, the inclusion of Rashba SOC can strongly enhance the low-bias conductance. To understand the origin of this SOC effect, and similar trends from Sec. II, we note that in the normal state for the barrier region the dispersion is SOC split and shifted by the barrier potential (assuming $V_0 > 0$). As in Sec. II, a spinor of an incident electron with $k_\parallel$ can be decomposed into barrier eigenspinors $|\chi_\sigma\rangle = \langle\chi_+|\chi_\sigma\rangle|\chi_+\rangle + \langle\chi_-|\chi_\sigma\rangle|\chi_-\rangle$, where $\chi_\pm$ from Eq. (27) has helicity ±1. The two helicities have *inequivalent* effective barriers [recall Eqs. (13) and (14)]

$$Z_\pm = Z \pm \lambda k_\parallel/2k_F. \quad (33)$$

Since $Z, \lambda k_\parallel/(2k_F) \geqslant 0$, for positive helicity the barrier is enhanced $Z_{eff}^+ \geqslant Z$. However, for negative helicity, at $Z = \lambda k_\parallel/(2k_F)$, Z_- becomes effectively completely transparent, such $k_\parallel$ can be viewed as "open channels" and are responsible for a strongly increased dI/dV.

Some peculiar conductance trends can already be understood at $V = 0$ and $T = 0$ K, where the charge transport in F/S junctions is determined by conventional and spin-flip Andreev reflection with opposite and equal spin projection of the incident and reflected particle, respectively, corresponding to the spin-singlet and spin-triplet interfacial superconducting correlations. For $G(V = 0)$ plotted in the plane defined by $Z > 0$ and $\lambda > 0$, a striking behavior was found for $|P| < 1$ in the triangular region approximately delimited with lines T1 and T2 [33],

$$\text{T1: } \lambda = 2Z/\sqrt{1 - P}, \quad \text{T2: } \lambda = 2Z, \quad (34)$$

where G is dominated by the spin-flip Andreev reflection and proximity-induced spin-triplet superconductivity.

Before showing next that a region in G delimited by the lines T1 and T2 also pertains to the enhanced calculated MAAR, we comment on relaxing the assumption of equal masses and Fermi velocities in the F and S regions. In a simple 1D N/S case, without SOC, different Fermi velocities $F_v = (v_S/v_N) \neq 1$ are known to increase the effective barrier strength $Z_{eff}^2 \to Z^2 + (1 - F_v)^2/4F_v > Z^2$ [41]. While this argument is often used to also ignore a Fermi velocity mismatch in the F/S case [52], as it is accounted for by simply enhancing Z, some subtleties exist [31,42]. The mismatch of effective masses $F_m = m_S/m_F$ together with the mismatch of the Fermi wave vectors $F_k = q_F/k_F$ can then be viewed as determining F_v and enhancing the effective Z. In our studies with SOC, $F_k \neq 1$ implies that Eq. (33) should be generalized by replacing k_F with $\sqrt{k_F q_F}$, including in the expression for open channels and a vanishing Z_-. Even with such a
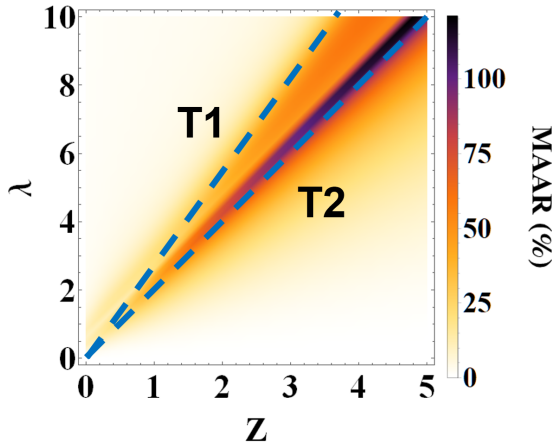
FIG. 7. Amplitude of out-of-plane magnetoanisotropic Andreev reflection (MAAR), given by Eq. (3) calculated at zero bias and $T = 0$ K, shown as a function of interfacial parameters Z and λ for $P = 0.47$, consistent with $Fe_{0.29}TaS_2$. Lines T1 and T2 are defined in Eq. (34).

wave-vector mismatch, the spin-triplet contribution remains enhanced within a triangular region, as long as $F_k > \sqrt{1 - P}$, i.e., $q_F > k_\downarrow$. The delimiting lines T1 and T2, for both $F_k < 1$ and $F_k > 1$, have slopes modified by F_k as compared to those given by Eq. (34).

V. F/S OUT-OF-PLANE MAAR

Just as in the F/2DEG structures, the interplay between exchange field and Rashba SOC will lead to various nonmonotonic trends [30,32,33,54]. Such trends can be inferred from Eqs. (33) and (34), as well as in the MR, which in F/S junctions corresponds to the superconducting counterpart of TAMR, and its term MAAR (recall Sec. I), identified the key role of the Andreev reflection.

Similar to the significance of the condition for perfect transmission and contour matching in understanding the origin of an enhanced TAMR, for MAAR it is important to identify the influence of open channels [33]. From Eq. (33), we see that $Z, \lambda > 0$ yields vanishing Z_- with open channels located at the Fermi contour of radius

$$k_\parallel^{\text{open}} = (2Z/\lambda)k_F. \quad (35)$$

Open channels give the dominant contribution to G and are also expected to determine the amplitude of MAAR.

Since evanescent states for large $k_\parallel$ do not contribute to G they should be excluded in open channels. From Snell's law [42], for the incident majority-spin electron this implies that to have propagating scattering states, $k_\parallel \leqslant k_\downarrow$ is required for conventional Andreev reflections and $k_\parallel \leqslant q_F$ for dominant spin-flip Andreev reflections [31]. The maximum of the total G is achieved when the amount of the open channels $\propto k_\parallel$ is maximized. For $k_F = q_F$, in the two limiting cases $k_\parallel^{\text{open}} = k_\downarrow$ and $k_\parallel^{\text{open}} = k_F$ we recover the conditions for lines T1 and T2 from Eq. (34), such that the maximum spin-flip Andreev reflection is located near $k_\parallel^{\text{open}} = k_F$, i.e., $\lambda = 2Z$.

From the calculated MAAR in Fig. 7 we see that the triangular region delimited by lines T1 and T2 is also

identifying the region of an enhanced MAAR and confirming the influence of open channels. Similar to our contour matching in TAMR, as noted in Sec. II, for a full picture the role of spin mismatch also needs to be included. Two characteristic features are easy to see from Fig. 7: (i) a large MAAR enhancement, which can reach 100 %, and (ii) MAAR is nonomontonic with both Z and λ, when the other parameter is kept constant.

To understand (i), we recall that in the triangular region, the dominant contribution to the total G is from the open channels that is associated with spin-flip Andreev reflection and spin-triplet pairing $|\uparrow\uparrow\rangle$. Therefore, the total conductance can be approximately written as

$$G(V = 0) \approx \int k_\parallel dk_\parallel \int_0^{2\pi} \frac{d\gamma}{\pi k_F^2} R_{\sigma=1}^h(k_\parallel, \gamma)$$

$$\approx k_\parallel^{\text{open}} \Delta k_\parallel \int_0^{2\pi} \frac{d\gamma}{\pi k_F^2} R_{\sigma=1}^h(k_\parallel^{\text{open}}, \gamma), \quad (36)$$

where $\Delta k_\parallel$ is the width of the open channels in $\boldsymbol{k}_\parallel$ plane, and γ is the angle between $\boldsymbol{k}_\parallel$ and $\hat{\boldsymbol{k}}_x$ [recall Eq. (27)]. For out-of-plane $\mathbf{M}$, $R_{\sigma=1}^h(k_\parallel^{\text{open}}, \gamma) \equiv R_{\sigma=1}^{h,\text{open}}$ does not depend on γ due to the rotational symmetry and we can write

$$G(\theta = 0) \approx \frac{2k_\parallel^{\text{open}} \Delta k_\parallel}{k_F^2} R_{\sigma=1}^{h,\text{open}}. \quad (38)$$

For in-plane $\mathbf{M}$, considering the interplay between the incident electron spin and the barrier eigenspinor, the spin-flip Andreev reflection of an incident $\uparrow$ electron is given by $R_{\sigma=1}^h(k_\parallel^{\text{open}}, \gamma) \approx R_{\sigma=1}^{h,\text{open}} \cos^2(\gamma - \phi)$ [33]. As a result, for in-plane $\mathbf{M}$, we obtain

$$G\left(\theta = \frac{\pi}{2}\right) \approx \frac{k_\parallel^{\text{open}} \Delta k_\parallel}{k_F^2} R_{\sigma=1}^{h,\text{open}} = \frac{G(\theta = 0)}{2}. \quad (39)$$

From Eq. (3), this means that MAAR in the triangular region is 100%, which explains that the previous prediction [32] can be attributed to spin-triplet superconductivity and is also consistent with the largest values in the experimental results for $Fe_{0.29}TaS_2$/NbN junctions with a perpendicular magnetic anisotropy [30].

Despite our simple theoretical model to include the interplay of exchange field and SOC on the proximity-induced superconductivity in F/S junctions, such a description provides MAAR which is in a good agreement with the measured angular dependence of MR in Fig. 8. Remarkably, just as the variation of Z shows a nonmonotonic MAAR in Fig. 7 and a huge increase of MAAR at intermediate Z values, which with Rashba SOC can lead to a vanishing Z_-, we see that this trend in Figs. 8(d), 8(e), and 8(h) is also retained in the measured results obtained by varying the Al_2O_3 barrier thickness ($\sim$1–2.5 nm).

While we cannot rule out a non-MAAR contribution in the measured low-bias MR for $Fe_{0.29}TaS_2$/NbN junctions, we can still examine its magnitude from several reported control measurements [30]. For example, by increasing T above T_c,
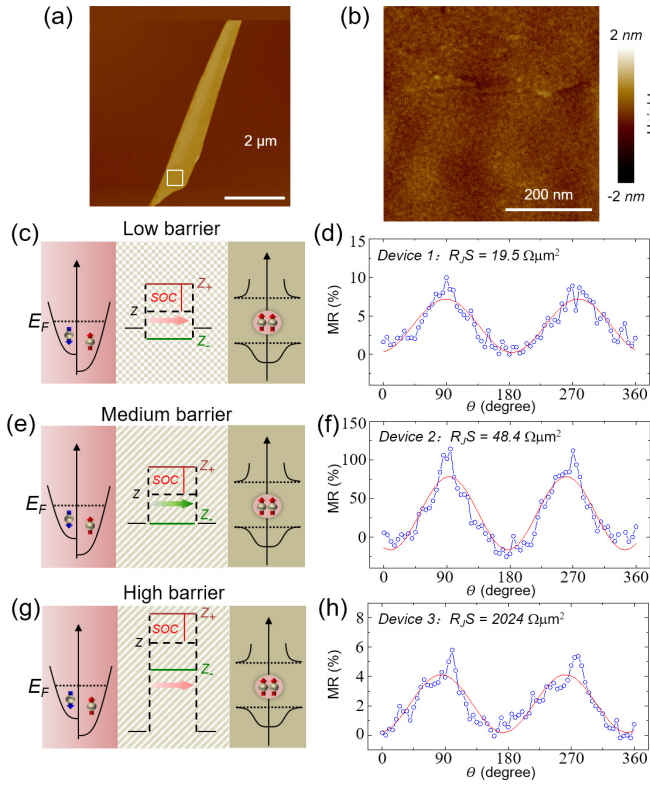
FIG. 8. (a), (b) Atomic force microscope images of 2-nm Al_2O_3 on $Fe_{0.29}TaS_2$ thin flake with rms roughness of ~ 0.270 nm indicate that Al_2O_3 is relatively flat and without obvious pin holes or discontinuities. (c), (e), (g) Schematic of the incident spin-polarized electrons tunneling across different effective interfacial barriers with Rashba SOC into the proximity-induced spin-triplet superconductivity. (d), (f), (h) The corresponding magnetoresistance (MR) (recall θ in Fig. 2), for different junction resistance-area products $R_J S$, a proxy for dimensionless barrier strength Z. Red lines: theoretically predicted twofold symmetry. The measurements were at $T = 2$ K, $B = 9$ T, and $V = 1$ mV.

MR is drastically reduced from its maximum at $\sim 100\%$ in Fig. 8(f) and we can attribute the main MR part to a superconducting response. By considering MR in $Al/Al_2O_3/NbN$ samples, we no longer have the interplay between the ferromagnetism and SOC, responsible for MAAR, but the resulting small MR of just few % at $T = 2$ K is encouraging that the presence of vortices at $B = 9$ T has only a modest MR effect. Taken together, these findings confirm that MAAR is indeed the dominant source of the measured MR in Fig. 8, which further indicates that $F_{0.29}TaS_2/NbN$ junctions provide an important platform to realize elusive equal-spin-triplet superconductivity.

VI. DISCUSSION AND CONCLUSIONS

We have shown that Rashba SOC can lead to strongly enhanced magnetoresistance in junctions with one ferromagnet. Both in the normal-state and the superconducting response the calculated magnetoresistance is characterized by various nonmonotonic trends. While some of these trends and an enhanced magnetoresistance have been measured in

superconducting junctions [30,55], experiments in the normal state are largely unexplored.

To realize magnetic proximity effects for the in-plane transport, magnetic insulators are desirable [23,56–58]. This precludes current flow in the more resistive F region [Fig. 1(a)] and minimizes hybridization with the 2DEG to enable a gate-tunable proximity-induced exchange splitting in their respective states. However, as shown in graphene [59–61] for tunable magnetic proximity effects one could also employ ferromagnetic metals, separated by an insulating layer from the 2DEG.

For a suitable materials platform, which would support large magnetoresistive effects, we could extend our focus on simple Rashba SOC to a growing class of van der Waals (vdW) materials. Their heterostructure offers both transport in materials with strong SOC as well 2D ferromagnets [62–64] with atomically sharp interfaces and not limited to lattice-matching constraints. For example, transition-metal dichalcogenides in addition to their inherent SOC also provide spin-orbit proximity [65–71] and thereby alter spin textures and expected TAMR, while 2D ferromagnets support a versatile gate control [72–74].

While we have focused on a longitudinal transport in a very simple system, the behavior emerging from a spin-parity-time symmetry of the scattering states with perfect transmission is important not just in explaining a surprisingly large TAMR, but also as a sensitive probe to distinguish between trivial and topological states [11]. It would be interesting to know if our predicted nonmonotonic trends with interfacial parameters for TAMR could be also relevant for other transport phenomena in junctions with a single ferromagnet, such as spin-orbit torque and spin-Hall magnetoresistance [5,75].

In the superconducting state, the observed large magnetoresistance has important implications as it provides an alternative probe for spin-triplet or mixed singlet-triplet superconductivity [76] and such a large signal is possible to realize even systems with only a modest SOC and negligible normal-state magnetoresistance [55]. Since this work shows that spin-triplet superconductivity, desirable both for superconducting spintronics and Majorana bound states [14], is feasible in simple structures with a single F and S region, it would also be important to extend its analysis to Josephson junctions, where enhanced magnetoresistance was predicted [77], but not connected to the spin-triplet superconductivity, which was extensively studied in other Josephson junctions [13,14,78–81].

In our work, the nonmonotonic trends with the interfacial barrier strength were observed by comparing samples with different thickness of the (Al_2O_3). It would be desirable to realize systems in which such changes, as well as the tunability of the Rashba SOC strength, could be controlled in the same sample. A desirable progress is realized in Josephson junctions where currently there are no ferromagnetic regions, but the Zeeman splitting is due to an applied magnetic field [14,82–86]. Related experimental support in junctions with Al as a superconductor and InAs-based 2DEG already suggests an observation of topological spin-triplet superconductivity [84]. In the same sample that both a reentrant superconductivity with an applied magnetic field and the jump in the superconducting phase are measured, but an enhanced

magnetoresistance as another signature of spin-triplet super-conductivity has not yet been studied.

ACKNOWLEDGMENTS

[1] S. Maekawa and U. Gafvert, Electron tunneling between ferro-magnetic films, IEEE Trans. Magn. **18**, 707 (1982).

[2] J. S. Moodera, L. R. Kinder, T. M. Wong, and R. Meservey, Large Magnetoresistance at Room Temperature in Ferromagnetic Thin Film Tunnel Junctions, Phys. Rev. Lett. **74**, 3273 (1995).

[3] I. Žutić, J. Fabian, and S. Das Sarma, Spintronics: Fundamentals and applications, Rev. Mod. Phys. **76**, 323 (2004).

[4] S. S. P. Parkin, C. Kaiser, A. Panchula, P. M. Rice, B. Hughes, M. Samant, and S.-H. Yang, Giant tunneling magnetoresistance at room temperature with MgO (100) tunnel barriers, Nat. Mater. **3**, 862 (2004).

[5] *Spintronics Handbook Spin Transport and Magnetism, 2nd Edition*, edited by E. Y. Tsymbal and I. Žutić (CRC Press, Boca Raton, FL, 2019).

[6] W. Thomson, On the electro-dynamic qualities of metals:– Effects of magnetization on the electric conductivity of nickel and of iron, Proc. R. Soc. London **8**, 546 (1857).

[7] C. Gould, C. Rüster, T. Jungwirth, E. Girgis, G. M. Schott, R. Giraud, K. Brunner, G. Schmidt, and L. W. Molenkamp, Tunneling Anisotropic Magnetoresistance: A Spin-Valve-Like Tunnel Magnetoresistance Using a Single Magnetic Layer, Phys. Rev. Lett. **93**, 117203 (2004).

[8] J. Moser, A. Matos-Abiague, D. Schuh, W. Wegscheider, J. Fabian, and D. Weiss, Tunneling Anisotropic Magnetoresistance and Spin-Orbit Coupling in Fe/GaAs/Au Tunnel Junctions, Phys. Rev. Lett. **99**, 056601 (2007).

[9] A. N. Chantis, K. D. Belashchenko, E. Y. Tsymbal, and M. van Schilfgaarde, Tunneling Anisotropic Magnetoresistance Driven by Resonant Surface States: First-Principles Calculations on an Fe(001) Surface, Phys. Rev. Lett. **98**, 046601 (2007).

[10] J. Fabian, A. Matos-Abiague, C. Ertler, P. Stano, and I. Žutić, Semiconductor spintronics, Acta Phys. Slov. **57**, 565 (2007).

[11] C. Shen, T. Leeney, A. Matos-Abiague, B. Scharf, J. E. Han, and I. Žutić, Resonant tunneling anisotropic magnetoresistance induced by magnetic proximity, Phys. Rev. B **102**, 045312 (2020).

[12] Yu. A. Bychkov and E. I. Rashba, Properties of a 2D with lifted spectral degeneracy, Zh. Eksp. Teor. Fiz. Pisma Red. **39**, 66 (1984) [JETP Lett. **39**, 78 (1984)].

[13] R. Cai, I. Žutić, and W. Han, Superconductor/ferromagnet heterostructures for superconducting spintronics and quantum computation, Adv. Quantum Technol. **6**, 2200080 (2023).

[14] M. Amudsen, J. Linder, J. W. A. Robinson, I. Žutić, and N. Banerjee, Colloquium: Spin-orbit effects in superconducting hybrid structures, arXiv:2210.03549.

[15] M. Eschrig, Spin-polarized supercurrents for spintronics: A review of current progress, Rep. Prog. Phys. **78**, 104501 (2015).

[16] J. Linder and J. W. A. Robinson, Superconducting spintronics, Nat. Phys. **11**, 307 (2015).

[17] A. I. Buzdin, Proximity effects in superconductor-ferromagnet heterostructures, Rev. Mod. Phys. **77**, 935 (2005).

[18] F. S. Bergeret, A. F. Volkov, and K. B. Efetov, Odd triplet superconductivity and related phenomena in superconductor-ferromagnet structures, Rev. Mod. Phys. **77**, 1321 (2005).

[19] A. Yu Kitaev, Unpaired Majorana fermions in quantum wires, Phys.-Usp. **44**, 131 (2001).

[20] D. Aasen, M. Hell, R. V. Mishmash, A. Higginbotham, J. Danon, M. Leijnse, T. S. Jespersen, J. A. Folk, C. M. Marcus, K. Flensberg, and J. Alicea, Milestones Toward Majorana-Based Quantum Computing, Phys. Rev. X **6**, 031016 (2016).

[21] U. Güngördü and A. A. Kovalev, Majorana bound states with chiral magnetic textures, J. Appl. Phys. **132**, 041101 (2022).

[22] K. Laubscher and J. Klinovaja, Majorana bound states in semiconducting nanostructures, J. Appl. Phys. **130**, 081101 (2021).

[23] I. Žutić, A. Matos-Abiague, B. Scharf, H. Dery, and K. Belashchenko, Proximitized materials, Mater. Today **22**, 85 (2019).

[24] I. A. Akimov, M. Salewski, I. V. Kalitukha, S. V. Poltavtsev, J. Debus, D. Kudlacik, V. F. Sapega, N. E. Kopteva, E. Kirstein, E. A. Zhukov, D. R. Yakovlev, G. Karczewski, M. Wiater, T. Wojtowicz, V. L. Korenev, Yu. G. Kusrayev, and M. Bayer, Direct measurement of the long-range *p-d* exchange coupling in a ferromagnet-semiconductor Co/CdMgTe/CdTe quantum well hybrid structure, Phys. Rev. B **96**, 184412 (2017).

[25] V. L. Korenev, I. V. Kalitukha, I. A. Akimov, V. F. Sapega, E. A. Zhukov, E. Kirstein, O. S. Ken, D. Kudlacik G. Karczewski, M. Wiater, T. Wojtowicz, N. D. Ilyinskaya, N. M. Lebedeva, T. A. Komissarova, Yu. G. Kusrayev, D. R. Yakovlev, and M. Bayer, Low voltage control of exchange coupling in a ferromagnet-semiconductor quantum well hybrid structure, Nat. Commun. **10**, 2899 (2019).

[26] K. Takiguchi, L. D. Anh, T. Chiba, T. Koyama, D. Chiba, and M. Tanaka, Giant gate-controlled proximity magnetoresistance in semiconductor-based ferromagnetic/non-magnetic bilayers, Nat. Phys. **15**, 1134 (2019).

[27] C. Betthausen, T. Dollinger, H. Saarikoski, V. Kolkovsky, G. Karczewski, T. Wojtowicz, K. Richter, and D. Weiss, Spin-transistor action via tunable Landau-Zener transitions, Science **337**, 324 (2012).

[28] D. J. Griffiths, *Introduction to Quantum Mechanics, Second Edition* (Pearson Prentice Hall, Upper Saddle River, NJ, 2005).

[29] J. J. Sakurai and J. Napolitano, *Modern Quantum Mechanics, Second Edition* (Addison-Wesley, San Francisco, CA, 2011).

[30] R. Cai, Y. Yao, P. Lv, Y. Ma, W. Xing, B. Li, Y. Ji, H. Zhou, C. Shen, S. Jia, X. C. Xie, I. Žutić, Q.-F. Sun, and W. Han, Evidence for anisotropic spin-triplet Andreev reflection at the 2D van der Waals ferromagnet/superconductor interface, Nat. Commun. **12**, 6725 (2021).

[31] I. Žutić and S. Das Sarma, Spin-polarized transport and Andreev reflection in semiconductor/superconductor hybrid structures, Phys. Rev. B **60**, R16322 (1999).

[32] P. Högl, A. Matos-Abiague, I. Žutić, and J. Fabian, Magnetoanisotropic Andreev Reflection in Ferromagnet-Superconductor Junctions, Phys. Rev. Lett. **115**, 116601 (2015).

[33] T. Vezin, C. Shen, J. E. Han, and I. Žutić, Enhanced spin-triplet pairing in magnetic junctions with *s*-wave superconductors, Phys. Rev. B **101**, 014515 (2020).

[34] P. Lv, Y.-F. Zhou, N.-X. Yang, and Q.-F. Sun, Magnetoanisotropic spin-triplet Andreev reflection in ferromagnet-Ising superconductor junctions, Phys. Rev. B **97**, 144501 (2018).

[35] R. Winkler, *Spin-Orbit Coupling Effects in Two-Dimensional Electron and Hole Systems* (Springer, New York, 2003).

[36] I. V. Rozhansky, N. S. Averkiev, and E. Lähderanta, Resonant tunneling between two-dimensional layers accounting for spin-orbit interaction, Phys. Rev. B **93**, 195405 (2016).

[37] H. Liu, E. Marcellina, A. R. Hamilton, and D. Culcer, Strong Spin-Orbit Contribution to the Hall Coefficient of Two-Dimensional Hole Systems, Phys. Rev. Lett. **121**, 087701 (2018).

[38] D. P. Arovas and Y. Lyanda-Geller, Non-Abelian geometric phases and conductance of spin-3/2 holes, Phys. Rev. B **57**, 12302 (1998).

[39] S. M. Girvin and K. Yang, *Modern Condensed Matter Physics* (Cambridge University Press, Cornwall, UK, 2019).

[40] G. E. Blonder, M. Tinkham, and T. M. Klapwijk, Transition from metallic to tunneling regimes in superconducting microconstrictions: Excess current, charge imbalance, and supercurrent conversion, Phys. Rev. B **25**, 4515 (1982).

[41] G. E. Blonder and M. Tinkham, Metallic to tunneling transition in Cu-Nb point contacts, Phys. Rev. B **27**, 112 (1983).

[42] I. Žutić and O. T. Valls, Tunneling spectroscopy for ferromagnet/superconductor junctions, Phys. Rev. B **61**, 1555 (2000).

[43] B. K. Nikolić, L. P. Zârbo, and S. Souma, Mesoscopic spin Hall effect in multiprobe ballistic spin-orbit-coupled semiconductor bridges, Phys. Rev. B **72**, 075361 (2005).

[44] B. Scharf, A. Matos-Abiague, J. E. Han, E. M. Hankiewicz, and I. Žutić, Tunneling Planar Hall Effect in Topological Insulators: Spin Valves and Amplifiers, Phys. Rev. Lett. **117**, 166806 (2016).

[45] B. G. Park, J. Wunderlich, D. A. Williams, S. J. Joo, K. Y. Jung, K. H. Shin, K. Olejnik, A. B. Shick, and T. Jungwirth, Tunneling Anisotropic Magnetoresistance in Multilayer-(Co/Pt)/AlO$_x$/Pt Structures, Phys. Rev. Lett. **100**, 087204 (2008).

[46] T. Uemura, Y. Imai, M. Harada, K. Matsuda, and M. Yamamoto, Tunneling anisotropic magnetoresistance in epitaxial CoFe/n-GaAs junctions, Appl. Phys. Lett. **94**, 182502 (2009).

[47] A. Griffin and J. Demers, Tunneling in the normal-metal-insulator-superconductor geometry using the Bogoliubov equations of motion, Phys. Rev. B **4**, 2202 (1971).

[48] S. Kashiwaya and Y. Tanaka, Tunneling effects on surface bound states in unconventional superconductors, Rep. Prog. Phys. **63**, 1641 (2000).

[49] S. Wu and K. V. Samokhin, Tunneling conductance of ferromagnet/noncentrosymmetric superconductor junctions, Phys. Rev. B **80**, 014516 (2009).

[50] A. Matos-Abiague and J. Fabian, Anisotropic tunneling magnetoresistance and tunneling anisotropic magnetoresistance: Spin-orbit coupling in magnetic tunnel junctions, Phys. Rev. B **79**, 155303 (2009).

[51] X.-Y. Yu, H.-L. Feng, G.-X. Gu, Y.-H. Liu, Z.-L. Li, T.-S. Xu, and Y.-Q. Li, Andreev reflection spectroscopy of ferromagnetic Fe$_{0.26}$TaS$_2$ with layered structure, Acta Phys. Sin. **68**, 247201 (2019).

[52] R. J. Soulen Jr., J. M. Byers, M. S. Osofsky, B. Nadgorny, T. Ambrose, S. F. Cheng, P. R. Broussard, C. T. Tanaka, J. Nowak, J. S. Moodera, A. Barry, and J. M. D. Coey, Measuring the spin polarization of a metal with a superconducting point contact, Science **282**, 85 (1998).

[53] S. P. Chockalingam, M. Chand, J. Jesudasan, V. Tripathi, and P. Raychaudhuri, Superconducting properties and Hall effect of epitaxial NbN thin films, Phys. Rev. B **77**, 214503 (2008).

[54] Y. Mizuno, T. Yokoyama, and Y. Tanaka, Theory of charge transport in ferromagnetic semiconductor/s-wave superconductor junction, Phys. Rev. B **80**, 195307 (2009).

[55] I. Martinez, P. Högl, C. González-Ruano, J. P. Cascales, C. Tiusan, Y. Lu, M. Hehn, A. Matos-Abiague, J. Fabian, I. Žutić, and F. G. Aliev, Interfacial Spin-Orbit Coupling: A Platform for Superconducting Spintronics, Phys. Rev. Appl. **13**, 014030 (2020).

[56] Z. Jiang, C. Z. Chang, C. Tang, P. Wei, J. S. Moodera, and J. Shi, Independent tuning of electronic properties and induced ferromagnetism in topological insulators with heterostructure approach, Nano Lett. **15**, 5835 (2015).

[57] P. Wei, F. Katmis, B. A. Assaf, H. Steinberg, P. Jarillo-Herrero, D. Heiman, and J. S. Moodera, Exchange-Coupling-Induced Symmetry Breaking in Topological Insulators, Phys. Rev. Lett. **110**, 186807 (2013).

[58] A. T. Lee, M. J. Han, and K. Park, Magnetic proximity effect and spin-orbital texture at the Bi$_2$Se$_3$/EuS interface, Phys. Rev. B **90**, 155103 (2014).

[59] P. Lazić, K. D. Belashchenko, and I. Žutić, Effective gating and tunable magnetic proximity effects in two-dimensional heterostructures, Phys. Rev. B **93**, 241401(R) (2016).

[60] K. Zollner, M. Gmitra, T. Frank, and J. Fabian, Theory of proximity-induced exchange coupling in graphene on hBN/(Co,Ni), Phys. Rev. B **94**, 155441 (2016).

[61] J. Xu, S. Singh, J. Katoch, G. Wu, T. Zhu, I. Žutić, and R. K. Kawakami, Spin inversion in graphene spin valves by gate-tunable magnetic proximity effect at one-dimensional contacts, Nat. Commun. **9**, 2869 (2018).

[62] C. Gong, L. Li, Z. Li, H. Ji, A. Stern, Y. Xia, T. Cao, W. Bao, C. Wang, Y. Wang, Z. Q. Qiu, R. J. Cava, S. G. Louie, J. Xia, and X. Zhang, Discovery of intrinsic ferromagnetism in two-dimensional van der Waals crystals, Nature (London) **546**, 265 (2017).

[63] B. Huang, G. Clark, E. Navarro-Moratalla, D. R. Klein, R. Cheng, K. L. Seyler, D. Zhong, E. Schmidgall, M. A. McGuire, D. H. Cobden, W. Yao, D. Xiao, P. Jarillo-Herrero, and X. Xu, Layer-dependent ferromagnetism in a van der Waals crystal down to the monolayer limit, Nature (London) **546**, 270 (2017).

[64] C. Gong and X. Zhang, Two-dimensional magnetic crystals and emergent heterostructure devices, Science **363**, eaav4450 (2019).

[65] A. Avsar, J. Y. Tan, T. Taychatanapat, J. Balakrishnan, G. K. W. Koon, Y. Yeo, J. Lahiri, A. Carvalho, A. S. Rodin, E. C. T. O'Farrell, G. Eda, A. H. Castro Neto, and B. Özyilmaz, Spin-orbit proximity effect in graphene, Nat. Commun. **5**, 4875 (2014).

[66] W. Yan, O. Txoperena, R. Llopis, H. Dery, L. E. Hueso, and F. Casanova, A two-dimensional spin field-effect switch, Nat. Commun. **7**, 13372 (2016).

[67] W. Han, R. K. Kawakami, M. Gmitra, and J. Fabian, Graphene spintronics, Nat. Nanotechnol. **9**, 794 (2014).

[68] A. Dankert and S. P. Dash, Electrical gate control of spin current in van der Waals heterostructures at room temperature, Nat. Commun. **8**, 16093 (2017).

[69] Z. Wang, D.-K. Ki, H. Chen, H. Berger, A. H. MacDonald, and A. F. Morpurgo, Strong interface-induced spin-orbit interaction in graphene on WS_2, Nat. Commun. **6**, 8839 (2015).

[70] L. Antonio Benitez, J. F. Sierra, W. Savero Torres, M. Timmermans, M. V. Costache, and S. O. Valenzuela, Investigating the spin-orbit interaction in van der Waals heterostructures by means of the spin relaxation anisotropy, APL Mater. **7**, 120701 (2019).

[71] K. Douli, M. D. Petrović, K. Zollner, P. Plechac, J. Fabian, and B. K. Nikolić, Proximity spin-orbit torque on a two-dimensional magnet within van der Waals heterostructure: Current-driven antiferromagnet-to-ferromagnet reversible nonequilibrium phase transition in bilayer CrI_3, Nano Lett. **20**, 2288 (2020).

[72] K. S. Burch, D. Mandrus, and J.-G. Park, Magnetism in two-dimensional van der Waals materials, Nature (London) **563**, 47 (2018).

[73] Y. Deng, Y. Yu, Y. Song, J. Zhang, N. Z. Wang, Z. Sun, Y. Yi, Y. Z. Wu, S. Wu, J. Zhu, J. Wang, X. H. Chen, and Y. Zhang, Gate-tunable room-temperature ferromagnetism in two-dimensional Fe_3GeTe_2, Nature (London) **563**, 94 (2018).

[74] W. Xing, Y. Chen, P. M. Odenthal, X. Zhang, W. Yuan, T. Su, Q. Song, T. Wang, J. Zhong, S. Jia, X. C. Xie, Y. Li, and W. Han, Electric field effect in multilayer $Cr_2Ge_2Te_6$: A ferromagnetic 2D material, 2D Mater. **4**, 024009 (2017).

[75] K. D. Belashchenko, A. A. Kovalev, and M. van Schilfgaarde, Interfacial contributions to spin-orbit torque and magnetoresistance in ferromagnet/heavy-metal bilayers, Phys. Rev. B **101**, 020407(R) (2020).

[76] L. P. Gor'kov and E. I. Rashba, Superconducting 2D System with Lifted Spin Degeneracy: Mixed Singlet-Triplet State, Phys. Rev. Lett. **87**, 037004 (2001).

[77] A. Costa, P. Högl, and J. Fabian, Magnetoanisotropic Josephson effect due to interfacial spin-orbit fields in superconductor/ferromagnet/superconductor junctions, Phys. Rev. B **95**, 024514 (2017).

[78] T. S. Khaire, M. A. Khasawneh, W. P. Pratt, Jr., and N. O. Birge, Observation of Spin-Triplet Superconductivity in Co-Based Josephson Junctions, Phys. Rev. Lett. **104**, 137002 (2010).

[79] J. W. A. Robinson, J. D. S. Witt, and M. G. Blamire, Controlled injection of spin-triplet supercurrents into a strong ferromagnet, Science **329**, 59 (2010).

[80] N. Banerjee, J. W. A. Robinson, and M. G. Blamire, Reversible control of spin-polarised supercurrents in ferromagnetic Josephson junctions, Nat. Commun. **5**, 4771 (2014).

[81] O. T. Valls, *Superconductor/Ferromagnet Nanostructures* (World Scientific, Hackensack, NJ, 2022).

[82] A. Fornieri, A. M. Whiticar, F. Setiawan, E. Portolés, A. C. C. Drachmann, A. Keselman, S. Gronin, C. Thomas, T. Wang, R. Kallaher, G. C. Gardner, E. Berg, M. J. Manfra, A. Stern, C. M. Marcus, and F. Nichele, Evidence of topological superconductivity in planar Josephson junctions, Nature (London) **569**, 89 (2019).

[83] H. Ren, F. Pientka, S. Hart, A. T. Pierce, M. Kosowsky, L. Lunczer, R. Schlereth, B. Scharf, E. M. Hankiewicz, L. W. Molenkamp, B. I. Halperin, and A. Yacoby, Topological superconductivity in a phase-controlled Josephson junction, Nature (London) **569**, 93 (2019).

[84] M. C. Dartiailh, W. Mayer, J. Yuan, K. S. Wickramasinghe, A. Matos-Abiague, I. Žutić, and J. Shabani, Phase Signature of Topological Transition in Josephson Junctions, Phys. Rev. Lett. **126**, 036802 (2021).

[85] T. Zhou, M. C. Dartiailh, K. Sardashti, J. E. Han, A. Matos-Abiague, J. Shabani, and I. Žutić, Fusion of Majorana bound states with mini-gate control in two-dimensional systems, Nat. Commun. **13**, 1738 (2022).

[86] A. Banerjee, O. Lesser, M. A. Rahman, H.-R. Wang, M.-R. Li, A. Kringhøj, A. M. Whiticar, A. C. C. Drachmann, C. Thomas, T. Wang, M. J. Manfra, E. Berg, Y. Oreg, A. Stern, and C. M. Marcus, Signatures of a topological phase transition in a planar Josephson junction, arXiv:2201.03453.

[87] E. Rashba, Talk presented at the Spintronics 2001: International Conference on Novel Aspects of Spin-Polarized Transport and Spin Dynamics in Washington, D.C. (chaired by one of us [88]) (unpublished).

[88] I. Žutić, Novel aspects of spin-polarized transport and spin dynamics, J. Supercond. **15**, 5 (2002).

[89] E. I. Rashba, Spintronics: Sources and challenge. Personal perspective, J. Supercond. **15**, 13 (2002).